Phase diagram for passive electromagnetic scatterers

Jeng Yi Lee[1] **and Ray-Kuang Lee**[1,2,*]

[1]*Institute of Photonics Technologies, National Tsing-Hua University, Hsinchu 300, Taiwan*
[2]*Physics Division, National Center for Theoretical Science, Hsinchu 300, Taiwan*

[*]rklee@ee.nthu.edu.tw

Abstract: With the conservation of power, a phase diagram defined by amplitude square and phase of scattering coefficients for each spherical harmonic channel is introduced as a universal map for any passive electromagnetic scatterers. Physically allowable solutions for scattering coefficients in this diagram clearly show power competitions among scattering and absorption. It also illustrates a variety of exotic scattering or absorption phenomena, from resonant scattering, invisible cloaking, to coherent perfect absorber. With electrically small core-shell scatterers as an example, we demonstrate a systematic method to design field-controllable structures based on the allowed trajectories in this diagram. The proposed phase diagram and inverse design can provide tools to design functional electromagnetic devices.

OCIS codes: (290.4020) Mie theory; (160.4670) Optical materials.

References and links

1. J. Shi, F. Monticone, S. Elias, Y. Wu, D. Ratchford, X. Li, and A. Alú, "Modular assembly of optical nanocircuits," Nat. Commun. **5**, 3896 (2014).
2. N. Engheta, "Circuits with light at nanoscales: optical nanocircuits inspired by metamaterials," Science **317**, 1698–1702 (2007).
3. M. I. Tribelsky, and B. S. Lukyanchuk, "Anomalous light scattering by small particles," Phys. Rev. Lett. **97**, 263902 (2006).
4. F. Monticone, C. Argyropoulos, and A. Alú, "Multi-layered plasmonic covers for comblike scattering response and optical tagging," Phys. Rev. Lett. **110**, 113901 (2013).
5. A. Alú and N. Engheta, "Polarizabilities and effective parameters for collections of spherical nanoparticles formed by pairs of concentric double-negative, single-negative, and/or double-positive metamaterial layers," J. Appl. Phys. **97**, 094310 (2005).
6. R. E. Hamam, A. Karalis, J. D. Joannopoulos, and M. Soljacic, "Coupled-mode theory for general free-space resonant scattering of waves," Phys. Rev. A **75**, 053801 (2007).
7. H. Noh, Y. Chong, A.D. Stone, and H. Cao, "Perfect coupling of light to surface plasmons by coherent absorption," Phys. Rev. Lett. **108**, 186805 (2012).
8. H. Noh, S.M. Popoff, and H. Cao, "Broadband subwavelength focusing of light using a passive sink," Opt. Express **21**, 17435–17446 (2013).
9. M. I. Tribelsky, "Anomalous light absorption by small particles," Europhys. Lett. **94**, 14004 (2011).
10. V. Grigoriev, N. Bonod, J. Wenger, and B. Stout, "Optimizing nanoparticle designs for ideal absorption of light," ACS Photonics **2**, 263–270 (2015).
11. A. Alú and N. Engheta, "Achieving transparency with plasmonic and metamaterial coatings," Phys. Rev. E **72**, 016623 (2005).
12. A. Alú and N. Engheta, "Plasmonic materials in transparency and cloaking problems: mechanism, robustness, and physical insights," Opt. Express **15**, 3318–3332 (2007).
13. S. Muhlig, M. Farhat, C. Rockstuhl, and F. Lederer, "Cloaking dielectric spherical objects by a shell of metallic nanoparticles," Phys. Rev. B **83**, 195116 (2011).

14. S. Muhlig, A. Cunningham, J. Dintinger, M. Farhat, S. B. Hasan, T. Scharf, T. Burgi, F. Lederer, and C. Rockstuhl, "A self-assembled three-dimensional cloak in the visible," Sci. Rep. **3**, 2328 (2013).
15. M. Farhat, S. Mhlig, C. Rockstuhl, and F. Lederer, "Scattering cancellation of the magnetic dipole field from macroscopic spheres," Opt. Express **20**, 13896–13906 (2012).
16. A. Alú and N. Engheta, "Cloaking a sensor," Phys. Rev. Lett. **102**, 233901 (2009).
17. Z. Ruan and S. Fan, "Superscattering of light from subwavelength nanostructures," Phys. Rev. Lett. **105**, 013901 (2010)
18. Z. Ruan and S. Fan, "Design of subwavelength superscattering nanospheres," Appl. Phys. Lett. **98**, 043101 (2011).
19. A. Mirzaei, A. E. Miroshnichenko, I. V. Shadrivov, and Y. S. Kivshar, "Superscattering of light optimized by a genetic algorithm," Appl. Phys. Lett. **105**, 011109 (2014).
20. N. M. Estakhri and A. Alú, "Minimum-scattering superabsorbers," Phys. Rev. B. **89**, 121416 (2014).
21. Z. Ruan and S. Fan, "Temporal coupled-mode theory for Fano resonance in light scattering by a single obstacle," J. Phys. Chem. C **114**, 7324 (2010).
22. K. R. Catchpole and A. Polman, "Plasmonic solar cells," Opt. Express **16**, 21793–21800 (2008).
23. X. Zhang, Y. L. Chen, R. S. Liu, and D. P. Tsai, "Plasmonic photocatalysis," Rep. Prog. Phys. **76**, 046401 (2013).
24. J.-Y. Lee, M.-C. Tsai, P.-C. Chen, T.-T. Chen, K.-L. Chan, C.-Y. Lee, and R.-K. Lee, "Thickness effects on light absorption and scattering for nano-particles in shape of hollow-spheres," J. Phys. Chem. C **119**, 25754–25760 (2015).
25. L. R. Hirsch, R. J. Stafford, J. A. Bankson, S. R. Sershen, B. Rivera, R. E. Price, J. D. Hazle, N. J. Halas, and J. L. West, "Nanoshell-mediated near-infrared thermal therapy of tumors under magnetic resonance guidance," Proc. Natl. Acad. Sci. U. S. A. **100**, 13549–13554 (2003).
26. M. I. Tribelsky, A. E. Miroshnichenko, Y. S. Kivshar, B. S. Lukyanchuk, and A. R. Khokhlov, "Laser pulse heating of spherical metal particles," Phys. Rev. X **1**, 021024 (2011).
27. Y. Pu, R. Grange, C. L. Hsieh, and D. Psaltis, "Nonlinear optical properties of core-shell nanocavities for enhanced second-harmonic generation," Phys. Rev. Lett. **104**, 207402 (2010).
28. S.-W. Chu, T.-Y. Su, R. Oketani, Y.-T. Huang, H.-Y. Wu, Y. Yonemaru, M. Yamanaka, H. Lee, G.-Y. Zhuo, M.-Y. Lee, S. Kawata, and K. Fujita, "Measurement of a saturated emission of optical radiation from gold nanoparticles: Application to an ultrahigh resolution microscope," Phys. Rev. Lett. **112**, 017402 (2014).
29. A. Mirzaei, I. V. Shadrivov, A. E. Miroshnichenko, and Y. S. Kivshar, "Cloaking and enhanced scattering of core-shell plasmonic nanowires," Opt. Express **21**, 10454–10459 (2013).
30. R. Fleury, J. Soric, and A. Alú, "Physical bounds on absorption and scattering for cloaked sensors," Phys. Rev. B. **89**, 045122 (2014).
31. M. Born and E. Wolf, *Principle of Optics*, 7th ed. (Cambridge University, 1999).
32. C. F. Bohren and D. R. Huffman, *Absorption and Scattering of Light by Small Particles* (Wiley, 1983).
33. S. A. Maier, *Plasmonics: Fundamentals and Applications* (Springer, 2007).
34. H.C. van de Hulst, *Light Scattering by Small Particles* (Dover, 1981).

---

1. Introduction

With state-of-the-art nano-optical technologies, there are renewed interests on having an efficient way to manipulate and design nanostructures with unusual electromagnetic properties [1, 2]. In particular, resonant scattering [3–6], coherent perfect absorption [7–10], invisible cloaking [11–16], subwavelength superscattering [17–19], and minimum-scattering superabsorbers [20, 21], are revealed in a single, isotropic, and multi-layered scatterer. These metastructures could be expected to serve as functional nano-devices with promising applications in light harvesting [22–24], heat generation by metal nanoparticles [25, 26], optical nanocircuits and nonlinear optical processes [27, 28].

To have exotic electromagnetic properties at subwavelength scale, a variety of specific conditions are asked to be satisfied. Undoubtedly, a better understanding in the scattering coefficients could provide an access to design nanostructures. In general, we need to consider information about scattering limitation, power assignment, scattered radiation pattern, and robustness on the corresponding extrinsic field response of real scatterers. For working frequency of interests, for example, many metals are associated with a strong dispersion in the visible spectra, that introduces real loss effects and suppresses desired functions [29, 30]. As possible mismatching in physical parameters may occur, it is natural to seek optimized invisible cloaks or performance boundary in a cloaked sensor with the consideration of intrinsic loss in reality [30].

In this paper, we study the general relation between amplitude and phase in the scattering coefficients for any passive electromagnetic scatterers. A phase diagram is introduced by imposing the power conservation on absorption cross section for each partial wave channel, which acts as a universal map to design passive scatterers. Not only all physically allowed regions can be defined to satisfy the intrinsic power conservation, but also all exotic electromagnetic properties in the literature can be illustrated in this phase diagram. Moreover, we take electrically small core-shell scatterers as an example to illustrate a systematic way in designing the composition of subwavelength-structures with required scattering and absorption properties.

2. Phase diagram for a passive scatterer

We consider a linearly polarized plane wave with time evolution $e^{-i\omega t}$ at the angular frequency ω, which is illuminating on a single spherical object. The object could be made of multiple layers of uniform and isotropic media with complex permittivity and permeability, denoted as $\varepsilon = \varepsilon' + i\varepsilon''$ and $\mu = \mu' + i\mu''$, respectively. Here, ε'' and μ'' are both assumed to be positive real numbers for a passive medium. Without loss of generality, the surrounding environment is taken as non-absorptive, non-magnetic, and free of external sources or currents, i.e., $\varepsilon_0 = \mu_0 = 1$. In the following, we express the electric field $\vec{E}$ and magnetic field $\vec{H}$ in the environment by two auxiliary vector potentials, i.e., the transverse magnetic (TM) and transverse electric (TE) modes, which are respectively generated by two scalar spherical wave equations. Each scalar functions can be built by an infinite series with unknown coefficients determined through boundary conditions. By following the conventional notations, let the scattering coefficients be C_n^{TM} and C_n^{TE} for the transverse magnetic (TM) and transverse electric (TE) modes in each spherical harmonic channel labeled by the index n, respectively [31–34]. The corresponding absorption and scattering cross-sections, σ^{abs} and σ^{scat}, defined as the total power absorbed and scattered by a single scatterer with respect to the unit intensity of incident plane wave, can be expressed as

$$
\begin{aligned}
\sigma^{\text{abs}} &\equiv \sum_{n=1}^{\infty} \sigma_n^{\text{abs(TE)}} + \sigma_n^{\text{abs(TM)}} \\
&= -\sum_{n=1}^{\infty} \frac{(2n+1)\lambda^2}{2\pi} (\text{Re}\{C_n^{\text{TM}}\} + |C_n^{\text{TM}}|^2 + \text{Re}\{C_n^{\text{TE}}\} + |C_n^{\text{TE}}|^2),
\end{aligned}
\tag{1}
$$

$$
\sigma^{\text{scat}} = \sum_{n=1}^{n=\infty} \frac{(2n+1)\lambda^2}{2\pi} (|C_n^{\text{TM}}|^2 + |C_n^{\text{TE}}|^2),
\tag{2}
$$

where λ is the wavelength of incident wave in vacuum. For a given radius of particle, denoted as a, the value of size parameter $2\pi a/\lambda$ determines how many terms in these two convergent series to be dominant [32]. Here, we define the partial absorption cross section for each spherical harmonic channel, labeled by n, as $\sigma_n^{\text{abs(TE,TM)}} \equiv -\frac{(2n+1)\lambda^2}{2\pi}(\text{Re}\{C_n^{\text{(TE,TM)}}\} + |C_n^{\text{(TE,TM)}}|^2)$, for TE or TM mode. We further express the scattering coefficient as $C_n^{\text{(TE,TM)}} = |C_n^{\text{(TE,TM)}}|\exp\{i\theta_n^{\text{(TE,TM)}}\}$, where the magnitude $|C_n^{\text{(TE,TM)}}|$ is a positive real value and $\theta_n^{\text{(TE,TM)}}$ is the corresponding phase. Due to the conservation of power, these partial absorption cross-sections would be equal or larger than zero in each spherical harmonic channel, $\sigma_n^{\text{abs(TE,TM)}} \geq 0$.

By decomposing into partial waves, in terms of each spherical channel, we can have a universal phase diagram for any passive electromagnetic scatterers, as shown in Fig. 1. Interestingly, even though we do not write down any exact formulas for the scattering coefficient, the range to support physical values for the amplitude square only exists within $0 \leq |C_n^{\text{(TE,TM)}}|^2 \leq 1$; while the phase is bound within $\pi/2 \leq \theta_n^{(TE,TM)} \leq 3\pi/2$, as illustrated in Fig. 1. It is worth to remark
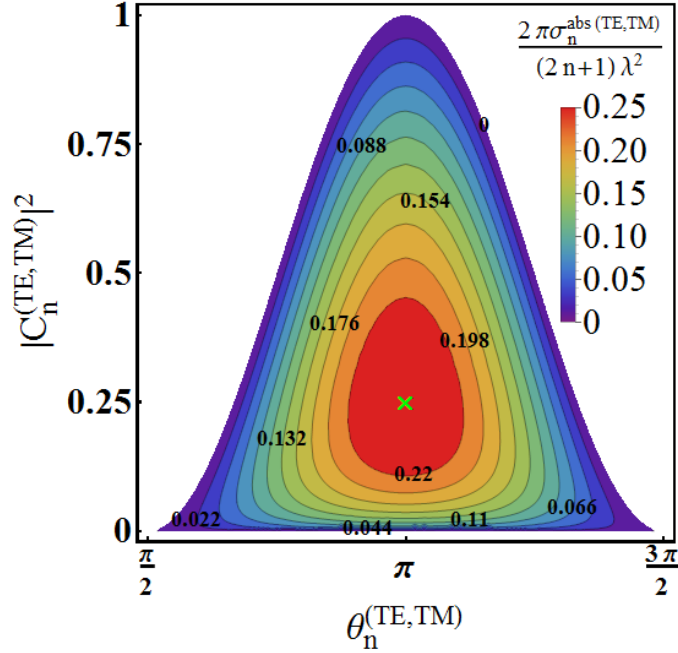
Fig. 1. A phase diagram for each spherical harmonic channel, labeled by n, is generated by imposing the power conservation on the partial absorption cross section, for TE or TM mode separately. Marked numbers shown in the contour lines correspond to the values of normalized absorption cross section in the individual channel: $\frac{2\pi}{(2n+1)\lambda^2}\sigma_n^{abs(TE,TM)}$. Colored regions are physically allowed solutions; while uncolored regions represent forbidden solutions. It is noted that the amplitude square is bounded within the range $[0,1]$; while the allowed phase is within $[\pi/2, 3\pi/2]$. The Green cross-marker, localed at $(\theta_n^{(TE,TM)} = \pi, |C_n^{(TE,TM)}|^2 = 0.25)$, indicates the maximum value, 0.25, in the normalized absorption cross-section.

that the range to support allowable solutions of scattering coefficients results from the intrinsic power conservation regardless of any specific scattering events. We depict the allowed solutions in colors for passive cases, which correspond to $\sigma_n^{abs(TE,TM)} \geq 0$ and depict the forbidden ones in white color for gain cases, which correspond to $\sigma_n^{abs(TE,TM)} < 0$. Along this lossless contour, there exist a family of solutions with the same value on $\sigma_n^{abs(TE,TM)} = 0$, but with different scattering coefficients in amplitude and phase. It is known that an ideally localized surface plasmon in the subwavelength structure relies on lossless resonance condition [3, 5], which corresponds to the point $|C_n^{(TE,TM)}| = 1$ and $\theta_n^{(TE,TM)} = \pi$ in our phase diagram. As for invisible cloaks [11–16], one can look for the solutions near bottom of the phase diagram, i.e., $|C_n^{(TE,TM)}| = 0$, for dominant channels.

Once the composited material in a scatterer has intrinsic loss, the scattering coefficients move to reside inside the colored region. For each channel, the maximum value in the normalized absorption cross section is $2\pi\sigma_n^{abs}/(2n+1)\lambda^2 = 1/4$, i.e., the Green cross-marker shown in Fig. 1, corresponding to coherent perfect absorbers [7–10], but which is also associated with the same amount of electromagnetic scattering power. The phase and amplitude of scattering coefficients to achieve a maximum absorption power is π and $1/2$, respectively. Moreover, along the contour for a constant absorption power, there exist a maximum and a minimum values in

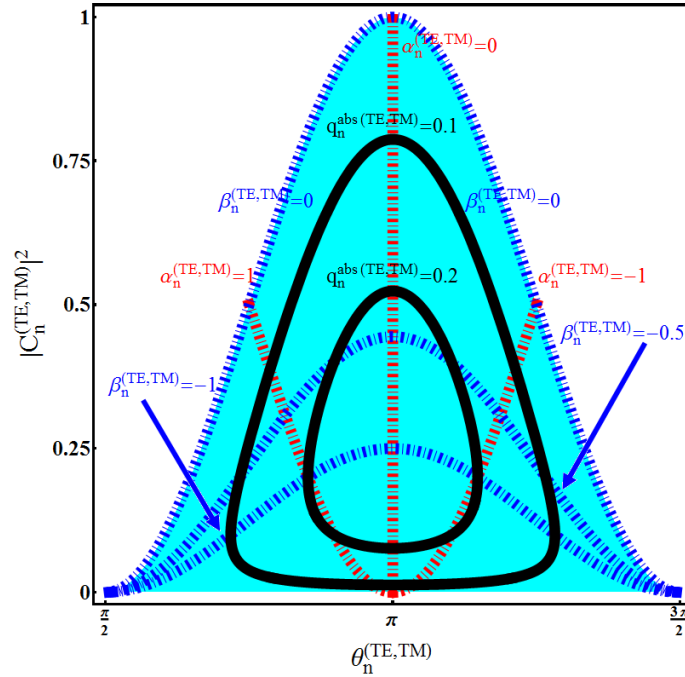Fig. 2. Supported trajectories in the phase diagram are shown for different sets of the parameters: $\alpha_n^{(TE,TM)}$ and $\beta_n^{(TE,TM)}$ defined in Eq. (3). Here, trajectories with a constant $\beta_n^{(TE,TM)}$ are shown in Blue dotted-dashed-curves; while trajectories with a constant $\alpha_n^{(TE,TM)}$ are shown in Red dotted-dashed-curves. Two contours for a constant absorption power are also depicted in the Black color.

the scattering amplitude, both at the phase $\theta_n^{(TE,TM)} = \pi$. It implies that one may design a scatterer possessing the same absorption power, but with different scattering signals. As for seeking an optimized "cloaking a sensor" [30], i.e., to have a better absorption efficiency with a constant absorption power, in the phase diagram one can follow the constant absorption contour to find the corresponding solution located at $\theta_n^{(TE,TM)} = \pi$ (conjugate-matched condition) with a minimum scattering amplitude.

3. From the trajectory in the phase diagram to design passive scatterers

Through above examples, the phase diagram provides a universal map to display all possible solutions for any passive scatterers. In principle, without knowing the composition in a scatterer, one can also have the same scattering coefficients. In this way, one may design specific scatterers with the required scattering and absorption properties by the choice of allowed trajectories in the phase diagram.

In the following, we introduce a systematic way to do the *inverse design* for the scatterer by specifying the required scattering or absorption properties. For a scatterer with N layers made of isotropic and homogeneous media, the corresponding scattering coefficient can be expressed in a compact form:

$$C_n^{(TE,TM)} = \frac{-1}{1 + i\frac{V_n^{(TE,TM)}}{U_n^{(TE,TM)}}} \equiv \frac{-1}{1 + i[\alpha_n^{(TE,TM)} + i\beta_n^{(TE,TM)}]}, \tag{3}$$
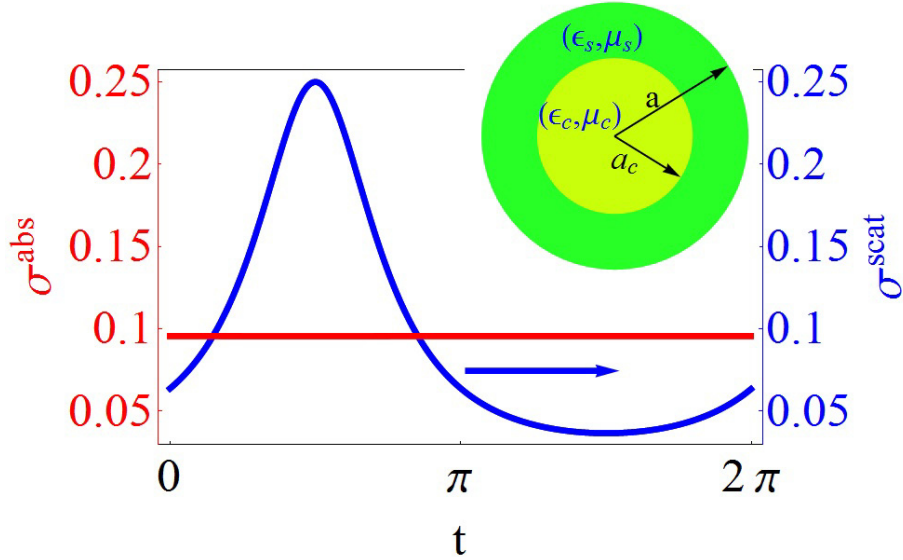
Fig. 3. Absorption and scattering cross sections correspond to the contour shown in Fig. 2, which are depicted in terms of the parametric variable t defined in Eqs. (4)-(5). Here, a constant absorption power is requested by setting $q_1^{TM} = 0.2$; while there is a degree of freedom in the scattering power. The insect illustrates the core-shell scatterer used as an example to design a passive electromagnetic devices with the constant absorption power.

where $U_n^{(TE,TM)}$ and $V_n^{(TE,TM)}$ are determinants of a $2N \times 2N$ matrix constituted by spherical harmonic functions [5,11,15,24]. Here, we also rewrite this scattering coefficient by introducing two auxiliary real numbers: $\alpha_n^{(TE,TM)}$ and $\beta_n^{(TE,TM)}$ in Eq. (3). By substituting Eq. (3) into the scattering coefficients, one can have different trajectories in the phase diagram, as illustrated in Fig. 2. Supported trajectories for the parameter sets with a constant value of $\alpha_n^{(TE,TM)}$ or $\beta_n^{(TE,TM)}$ are plotted in Red dotted-dashed- and Blue dotted-dashed-curves, respectively. The ranges to support allowable scattering solutions for passive scatterers on these numbers would be $\alpha_n^{(TE,TM)} = [-\infty, \infty]$ and $\beta_n^{(TE,TM)} = [-\infty, 0]$.

In particular, for the contour with a constant absorption power in the phase diagram, as shown in the Black color in Fig. 2, one can use the parametric representation of the curve to describe this supported trajectory. The corresponding parameter sets of $\alpha_n^{(TE,TM)}$ and $\beta_n^{(TE,TM)}$ can be found as

$$\alpha_n^{(TE,TM)}(t) = \sqrt{\frac{1}{4[q_n^{(TE,TM)}]^2} - \frac{1}{q_n^{(TE,TM)}}} \, \sin(t), \qquad (4)$$

$$\beta_n^{(TE,TM)}(t) = [1 - \frac{1}{2q_n^{(TE,TM)}}] + \sqrt{\frac{1}{4[q_n^{(TE,TM)}]^2} - \frac{1}{q_n^{(TE,TM)}}} \, \cos(t). \qquad (5)$$

Here, the independent variable, t, is used for the parametric equation, which is also bounded within the range $t = [0, 2\pi]$. For a given normalized absorption power, $q_n^{(TE,TM)} \equiv \frac{2\pi}{(2n+1)\lambda^2} \sigma_n^{abs(TE,TM)}$ in each channel, from Eqs. (4)-(5) one can see that the trajectory of $\alpha_n^{(TE,TM)}$ and $\beta_n^{(TE,TM)}$ in the phase diagram is following the request for a constant absorption power.

As an example, we consider a passive scatterer in the configuration of a core-shell sphere, as illustrated in the insect of Fig. 3, which is composed by two concentric layers of isotropic and homogeneous materials. The geometrical parameters and material properties for this core-shell scatterer are the radius of core, a_c, the radius of whole particle, a, and $\varepsilon_s(\mu_s)/\varepsilon_c(\mu_c)$ for the permittivity (permeability) in the shell/core regions, respectively. We limit our system to non-magnetic case, so $\mu_s = \mu_c = 1$. If the electrically small approximation is satisfied for such a core-shell scatterer, it is known that the main contribution dominantly comes from the electric dipole-wave scattering, i.e., $n = 1$ and TM mode. We choose the constant absorption power with $q_1^{(TM)} = 0.2$ in Eqs. (4)-(5). For such a two-layered scatterer, the corresponding scattering coefficients are conducted from a 4×4 matrix by tracking TE and TM modes. By applying the continuity of electric and magnetic fields established at the two boundaries of shell-environment and core-shell, one can approximately express the term V_1^{TM}/U_1^{TM} as

$$\frac{V_1^{TM}}{U_1^{TM}} = \frac{3\lambda^3}{2(2\pi a)^3} \frac{2\gamma^3(1-\varepsilon_s)(\varepsilon_c-\varepsilon_s)-(2+\varepsilon_s)(\varepsilon_c+2\varepsilon_s)}{\gamma^3(\varepsilon_s-\varepsilon_c)(2\varepsilon_s+1)+(1-\varepsilon_s)(\varepsilon_c+2\varepsilon_s)}, \tag{6}$$

where γ is defined as the ratio between the core radius to the whole particle radius, $\gamma \equiv a_c/a$. If one replaces ε by μ, then we can obtain the other term V_1^{TE}/U_1^{TE}. However for non-magnetic media it is automatically zero for $\mu_0 = \mu_s = \mu_c = 1$. By taking $\gamma = 1$ or $\varepsilon_s = \varepsilon_c$, above result can be reduced to the electric dipole equation for a solid sphere.

Now, for our core-shell system with the geometric size fixed, we provide a systematic way to find out the corresponding material properties with a constant absorption power, as specified by the contour in the phase diagram shown in Fig. 2. To give a clear illustration, first, one may fix the material property in the shell or in the core region. If we assume that the composition for the shell region is given, i.e., ε_s is fixed, then, based on Eqs. (4)-(6), the corresponding solution for the permittivity in the core region is found to satisfy:

$$\varepsilon_c = \varepsilon_s \frac{3(-2\varepsilon_s-4-2\gamma^3+2\gamma^3\varepsilon_s)-2(\alpha_1^{TM}+i\beta_1^{TM})(2\pi a/\lambda)^3(2-2\varepsilon_s+2\varepsilon_s\gamma^3+\gamma^3)}{3(\varepsilon_s+2+2\gamma^3\varepsilon_s-2\gamma^3)+2(\alpha_1^{TM}+i\beta_1^{TM})(2\pi a/\lambda)^3(1-\varepsilon_s-2\varepsilon_s\gamma^3-\gamma^3)}. \tag{7}$$

Solutions obtained from the analytical formula in Eq. (7) are shown in Figs. 4(a) and 4(b) for the real and imaginary parts of the permittivity in the core region, respectively. In terms of the parametric variable, t, we can have a wide rang in selecting core materials, and all of them have the same absorption power. Moreover, based on these found parameters, the corresponding absorption and scattering cross sections would satisfy our request for a constant absorption power, as shown in Fig. 3. From the comparison between Fig. 3 and Figs. 4(a)-4(b), we find that when $t = \pi/2$ the scattering power reaches a maximum value; while the ε_c'' for the required material has a minimum value, due to the reason that dissipative loss is proportional to the local electric field. In this scenario, with the help of a strong electric field, it becomes possible to maintain the same absorption power simultaneously.

On other hand, if the material property in the core region is specified, based on Eqs. (4)-(6) the corresponding solutions for the permittivity in the shell region ε_s to support a constant absorption power are governed by

$$\varepsilon_s^{\pm} = \frac{-g \pm \sqrt{g^2-4fh}}{2f}, \tag{8}$$

with the shorthanded notations:

$$f = 2(1-\gamma^3)[3-2(\alpha_1^{TM}+i\beta_1^{TM})(2\pi a/\lambda)^3], \tag{9}$$
$$g = 2(\alpha_1^{TM}+i\beta_1^{TM})(2\pi a/\lambda)^3[\gamma^3(1-2\varepsilon_c)+2-\varepsilon_c]+3(2\gamma^3+2\gamma^3\varepsilon_c+\varepsilon_c+4), \tag{10}$$
$$h = \varepsilon_c(1-\gamma^3)[6+2(\alpha_1^{TM}+i\beta_1^{TM})(2\pi a/\lambda)^3]. \tag{11}$$
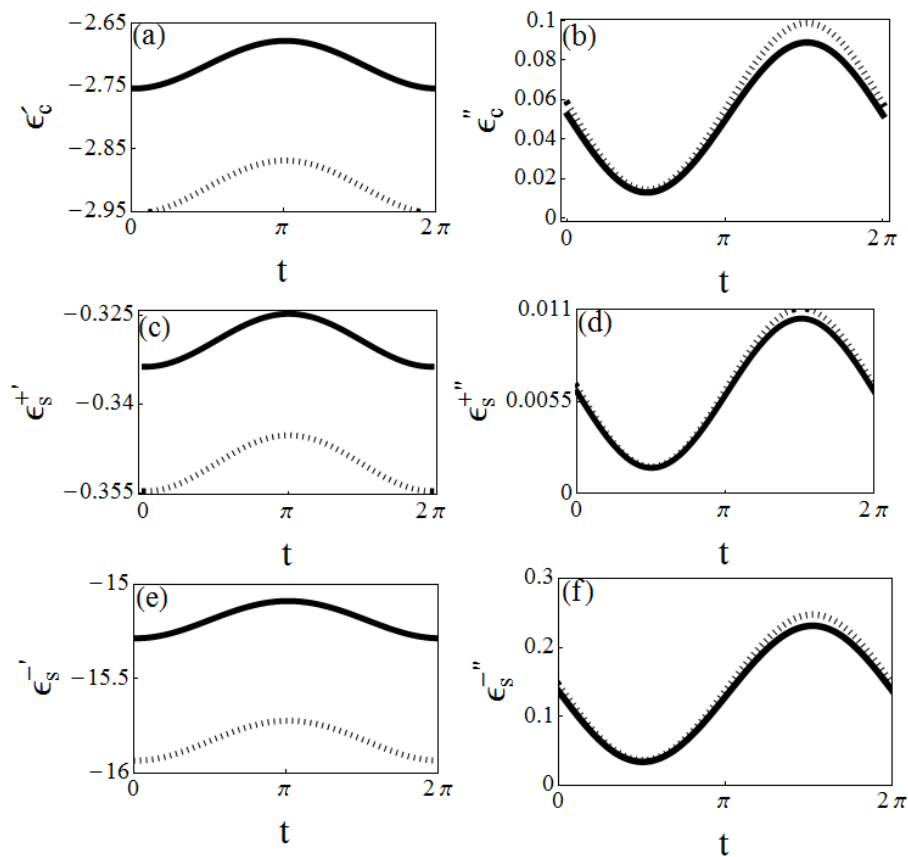
Fig. 4. The permittivities to support a constant absorption power are shown as a function of the parametric variable t. For a given material in the shell region, $\varepsilon_s = 3.12$, found solutions for the real and imaginary parts of the permittivity in the core region are shown in (a) and (b), respectively. For a given material in the core region, $\varepsilon_c = 5$, two families of found solutions shown in Eq. (8) are denoted as ε_s^+ and ε_s^- for the shell region, with the corresponding real and imaginary parts of the permittivity shown in (c, e) and (d, f), respectively. Results obtained from analytical formulas are depicted in solid-curves; while exact solutions from scattering theory are depicted in dashed-curves. In all cases, the core-shell geometries are fixed with $a = 1/24\lambda$ and $\gamma = 0.9$.

Derivations to have solutions in Eqs. (7) and (8) are shown in Appendix.

From Eq. (8), there exist two families to support the materials in the shell region, denoted as $\varepsilon_s^{\pm}$. We show the real and imaginary parts of the permittivity in the shell region for these two families in Figs. 4(c)-4(d) and 4(e)-4(f), as well as the exact solutions in dashed-curves, respectively. We reveal a good agreement between our analytical solutions and the numerical ones obtained by the exact scattering theory. Again, based on these results, the corresponding absorption and scattering cross sections would satisfy our request for a constant absorption power, as shown in Fig. 3. It is surprised to find that there exist a variety of choices for the material properties even a specific scattering or absorption property is given in the beginning. Without the introduction of this phase diagram and the inverse design, it is not only difficult to find out the required material properties, but also complicated to recognize the power competition and limitation among these cross sections for each channel.

Before concluding, we remark that when the electrically small approximation is not valid, multiple channels for TE and TM modes may be excited as expected. In this scenario, one can also apply our phase diagram, but not for a single channel only. By embedding multi-layered coatings to excite multiple channels, the intrinsic single channel limitation can be broken to generate superscattering or superabsorber phenomena [17–21, 29]. Scattering coefficients from several dominant channels are just a natural extension by considering all of them onto the phase diagrams simultaneously. In addition, although the proposed phase diagram is based on the well-known scattering formulas for symmetrically spherical scatterers, the concept of our phase diagram can be applied to non-spherical scatterers as well. Although in our example of inverse design we use well-known electric dipole formulas for core-shell systems, our approach to find out the corresponding materials for a given request on the scattering and absorption properties is always non-trivial. Through this universal phase diagram, one can have a systematic way to design functional passive electromagnetic scatterers.

4. Conclusion

In summary, we introduce a phase diagram as a compact tool to link the scattering and absorption powers for each spherical harmonic channel. Intrinsically, the power conservation for any passive scatterers gives the physically allowable solutions in the scattering coefficient. Not only the known exotic scattering and absorption phenomena can be illustrated in this diagram, but supported trajectories are also demonstrated to design extrinsic-field-controllable scatterers. With the core-shell scatterers at the subwavelength scale as an example, we reveal a systematic way to find out a variety of solutions in the composited materials to possess the same absorption power. In general, one can easily extend this methodology to go beyond the small particle size limitation, by considering interferences from several channels in the map. With the analogy among wave phenomena, the concept of this phase diagram and our inverse design method can be ready applied to acoustic systems as well as quantum scattering system.

Appendix

In this Appendix, we provide the formula to derive Eqs. (7) and (8) in detail. When the electrically small condition (quasi-static limit) is satisfied in a non-magnetic core-shell structure, the dominant scattered wave can be approximated by Eq. (6) [5, 11, 15, 24]. Then, by defining $Z_1^{TM} \equiv \alpha_1^{TM} + i\beta_1^{TM}$ as a shorthanded notation, Eq. (6) becomes

$$\frac{V_1^{TM}}{U_1^{TM}} = Z_1^{TM} = \frac{3}{2}\left(\frac{\lambda}{2\pi a}\right)^3 \frac{2\gamma^3(1-\varepsilon_s)(\varepsilon_c-\varepsilon_s)-(2+\varepsilon_s)(\varepsilon_c+2\varepsilon_s)}{\gamma^3(\varepsilon_s-\varepsilon_c)(2\varepsilon_s+1)+(1-\varepsilon_s)(\varepsilon_c+2\varepsilon_s)}. \qquad (12)$$

With the help of Eq. (12), one has

$$\varepsilon_c\{2(\frac{2\pi a}{\lambda})^3 Z_1^{TM}\left[-2\varepsilon_s\gamma^3-\gamma^3+1-\varepsilon_s\right]-3\left[2\gamma^3-2\gamma^3\varepsilon_s-2-\varepsilon_s\right]\} \tag{13}$$

$$=3\left[-4\varepsilon_s-2\varepsilon_s^2-2\gamma^3\varepsilon_s+2\gamma^3\varepsilon_s^2\right]-2(\frac{2\pi a}{\lambda})^3 Z_1^{TM}\left[\gamma^3(2\varepsilon_s^2+\varepsilon_s)+(2\varepsilon_s-2\varepsilon_s^2)\right],$$

which gives us the result in Eq. (7). Similar process can be applied to derive Eq. (8) by expanding every terms and collecting coefficients of ε_s, i.e.,

$$\varepsilon_s^2(2\gamma^3-2)\left[2(\frac{2\pi a}{\lambda})^3 Z_1^{TM}-3\right]+\left[2(\frac{2\pi a}{\lambda})^3 Z_1^{TM}\varepsilon_c(1-\gamma^3)-6\varepsilon_c(\gamma^3-1)\right] \tag{14}$$

$$+\varepsilon_s\left[2(\frac{2\pi a}{\lambda})^3 Z_1^{TM}(\gamma^3-2\varepsilon_c\gamma^3+2-\varepsilon_c)+3(2\gamma^3+2\gamma^3\varepsilon_c+4+\varepsilon_c)\right]=0.$$

Finally, with the shorthanded notations introduced in Eqs. (9)-(11), we have

$$f\varepsilon_s^2+g\varepsilon_s+h=0. \tag{15}$$

As a result, one can easily solve ε_s in Eq. (15), which gives the solutions shown in Eq. (8).

Acknowledgments